A Bipolar Spindle of Antiparallel ParM Filaments Drives Bacterial Plasmid Segregation

P. Gayathri *et al.*

Science **338**, 1334 (2012);
DOI: 10.1126/science.1229091

Science (print ISSN 0036-8075; online ISSN 1095-9203) is published weekly, except the last week in December, by the American Association for the Advancement of Science, 1200 New York Avenue NW, Washington, DC 20005.

A Bipolar Spindle of Antiparallel ParM Filaments Drives Bacterial Plasmid Segregation

P. Gayathri,[1] T. Fujii,[2]* J. Møller-Jensen,[1]† F. van den Ent,[1] K. Namba,[2,3] J. Löwe[1]‡

To ensure their stable inheritance by daughter cells during cell division, bacterial low-copy-number plasmids make simple DNA segregating machines that use an elongating protein filament between sister plasmids. In the ParMRC system of the *Escherichia coli* R1 plasmid, ParM, an actinlike protein, forms the spindle between ParRC complexes on sister plasmids. By using a combination of structural work and total internal reflection fluorescence microscopy, we show that ParRC bound and could accelerate growth at only one end of polar ParM filaments, mechanistically resembling eukaryotic formins. The architecture of ParM filaments enabled two ParRC-bound filaments to associate in an antiparallel orientation, forming a bipolar spindle. The spindle elongated as a bundle of at least two antiparallel filaments, thereby pushing two plasmid clusters toward the poles.

During bacterial cell division, an equal distribution of replicated plasmids to daughter cells ensures their stable inheritance. Low-copy-number plasmids encode the simplest known DNA segregation machines to perform this task. They comprise a nucleotide-driven (cytomotive) protein filament and a centromere-like DNA region, linked by an adaptor protein. The ParMRC segregation system of *Escherichia coli* R1 plasmid consists of ParM, an actinlike cytomotive protein (*1*) that forms polar, left-handed, double-helical filaments (*2*); ParR, an adaptor protein; and *parC*, a centromeric region (*3*, *4*). Dynamic instability of ParM filaments enables plasmid segregation by a "search and capture" mechanism (*5*, *6*), with ParRC (*7*, *8*) stabilizing the filaments. It has been reported that ParRC binds to both ends of a single ParM filament (*9*, *10*). This leads to a conundrum: How does ParRC bind to two different ends of a polar ParM filament?

Here, we provide a comprehensive description of ParM in the monomeric and filament states. An electron cryomicroscopy (cryo-EM) reconstruction (*11*) (Fig. 1A) provided a subnanometer-resolution map of the polar filament of ParM (resolution of 8.5 Å at FSC 0.5; fig. S1, A to D), polymerized in the presence of adenylyl-imidodiphosphate [AMPPNP, a nonhydrolyzable adenosine triphosphate (ATP) analog]. We determined the crystal structures of a nonpolymerizing mutant, ParM(Leu^{163}→Arg^{163}, L163R), bound to AMPPNP and ParM(Leu^{163}→Ala^{163}, L163A) bound to the C-terminal 17-residue peptide corresponding to the ParM-interacting region of ParR (*8*, *10*) (ParR$_{pept}$) and AMPPNP (*11*). Comparison of the crystal structures, including the previously reported apo- and adenosine diphosphate (ADP)–bound forms (*1*), revealed no large differences between the ATP and ADP states of

[1]Medical Research Council (MRC) Laboratory of Molecular Biology (LMB), Hills Road, Cambridge CB2 0QH, UK. [2]Graduate School of Frontier Biosciences, Osaka University, 1-3 Yamadaoka, Suita, Osaka 565-0871, Japan. [3]Riken Quantitative Biology Center, 1-3 Yamadaoka, Suita, Osaka 565-0871, Japan.

*Present address: Riken Quantitative Biology Center, 1-3 Yamadaoka, Suita, Osaka 565-0871, Japan.
†Present address: University of Southern Denmark, Campusvej 55, DK-5230 Odense, Denmark.
‡To whom correspondence should be addressed. E-mail: jyl@mrc-lmb.cam.ac.uk

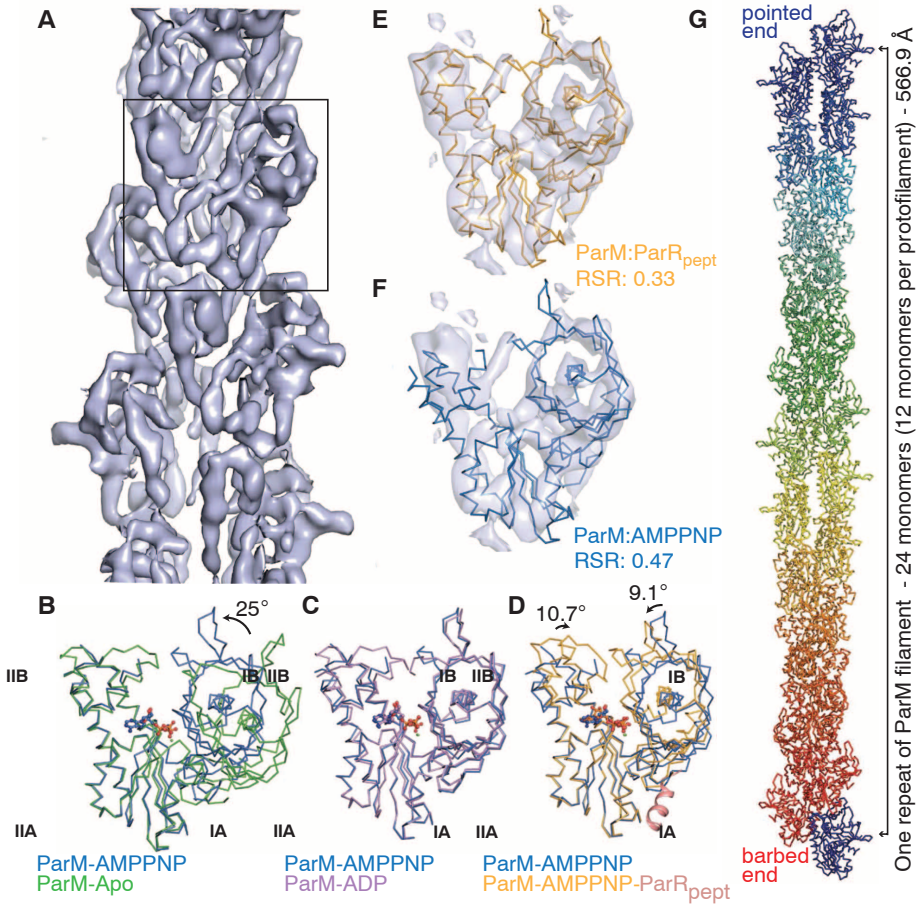

Fig. 1. Conformational cycle of ParM. (**A**) Cryo-EM reconstruction of the ParM filament. Box indicates a monomeric segment. (**B** to **D**) Superposition (using Cα atoms of domain IIA) of the conformations of ParM with the ParM-AMPPNP state (blue; PDB ID: 4A61): (B) unliganded ParM [green (*1*); PDB ID: 1MWK], (C) ParM-ADP state [magenta; (*1*); PDB ID: 1MWM], and (D) ParM with ParR$_{pept}$ and AMPPNP (orange; ParR$_{pept}$ in pink cartoon representation; PDB ID: 4A62). Domain rotations are indicated. (**E** and **F**) Rigid-body fit of ParM monomeric states into the cryoEM reconstruction. Domain I residues were fitted by using Chimera (*24*). Real-space R-factors (RSR) against the map for ParM:AMPPNP (E) and ParM:ParR$_{pept}$ (F) quantify the best fit (movie S1 and fig. S1E). (**G**) A repeat unit of the ParM filament (EMDB: EMD-1980, PDB ID: 4A6).

ParM monomers (Fig. 1, B and C). In contrast, domains IB and IIB showed a rotation of 9.1° and 10.7° toward the nucleotide-binding pocket (Fig. 1D) in the ParM:$ParR_{pept}$ structure, compared with the free monomer. The domain rotations were reminiscent of the transition from G-actin to F-actin (*12*, *13*). Fitting the monomeric structures of ParM into the cryo-EM reconstruction showed that the ParM:$ParR_{pept}$ structure fits best (Fig. 1, E and F, fig. S1E, and movie S1). Thus, the filament conformation of ParM is very similar to ParM:$ParR_{pept}$. The best fit provided a quasi-atomic model of the ParM filament (Fig. 1G) and implies that binding of ParR or ParR*C* locks ParM monomers in the filament-like conformation.

$ParR_{pept}$ was bound in a hydrophobic pocket between domains IA and IIA of ParM (Fig. 2A and fig. S2). The ParM-$ParR_{pept}$ interaction resembled proteins that bind at the barbed end of actin (Fig. 2, A and B). Many actin-binding proteins, including formins (*14*) and Wiskott-Aldrich homology domain 2–containing proteins such as Spire (*15*), insert a helix between the corresponding subdomains 1 and 3 of actin (*16*). The ParM:$ParR_{pept}$ structure modeled onto the ParM filament highlighted a substantial clash between $ParR_{pept}$ and residues 37 to 46 of the next ParM monomer in the protofilament (Fig. 2C). Thus, the ParR-binding site lies within the polymerization interface of ParM, and bound ParR needs to be replaced during elongation. Overlap in the binding site of $ParR_{pept}$ and the polymerization interface occludes all the ParR*C*-binding sites on the ParM filament except those at the barbed end, implying that ParR*C* binds exclusively to this end.

Our ParM-$ParR_{pept}$ structure supports a formin-like mechanism for the processive movement of ParR*C* (fig. S3). Ten ParR dimers bind *parC* repeats (*7*, *8*), forming a scaffold that allows a forminlike stair-stepping mechanism (fig. S3, B and C) (*17*). The C-terminal helices from the 20 ParRs are localized in a confined area. This probably facilitates ParM filament nucleation by ParR*C* (*18*). It also ensures ParR*C*-bound ParM monomer recruitment upon ParR displacement from the filament (fig. S3D), explaining end tracking of ParM filaments by ParR*C* through insertional polymerization (*6*, *19*). The ParR*C* cap locks the terminal monomers in the filament conformation, thus protecting the filament from dynamic instability.

To confirm the proposed single-end binding of ParR*C*, we examined the effect of ParR*C* on ParM filament elongation by using total internal reflection fluorescence (TIRF) microscopy (*11*). The experiments were performed with nonhydrolyzable AMPPNP to prevent dynamic instability. ParM-AMPPNP elongated symmetrically at both ends from an initial seed of the ParM filament (Fig. 3A and movie S2) (*5*). In the presence of unlabeled ParR*C*, one end of the filaments grew faster, resulting in asymmetric growth (Fig. 3B, fig. S4A, and movie S3). The rates of growth were 9.4 ± 4.1 and 2.5 ± 1.9 monomers per s (numbers after the ± symbol indicate standard deviation from the mean), for fast- and slow-growing ends (n = 32; table S3). Experiments with labeled ParR*C* showed that ParR*C* accelerated growth and recruited ParM monomers at the ParR*C*-bound filament end only (Fig. 3C, fig. S4B, and movie S4), reconfirming insertional polymerization (*6*). The unidirectional elongation by ParR*C* leads us to the key question: What enables bipolar plasmid segregation?

Frequent condensation events were observed between ParM filaments, both with ATP and AMPPNP (Fig. 4A and movies S5 to S8). Furthermore, continuous motion because of interfilament sliding occurred within filament bundles (Fig. 4B, fig. S4C, and movies S9 to S11). A molecular model for the filament sliding and condensation was generated on the basis of two monomers in the crystal packing of ParM:$ParR_{pept}$ (fig. S5A). ParM filament subunits, when superposed sequentially onto the ParM monomers, produced sliding and an antiparallel packing of filaments (Fig. 4C and fig. S5A). Mutation of residues within loop 18-21 [Ser^{19}→Arg^{19} and Gly^{21}→Arg^{21} (S19R and G21R)] at the proposed antiparallel filament interface (Fig. 4, C and D, and fig. S5B) prevented interfilament sliding (movie S12, Fig. 4E, and fig. S4D), because of stronger interactions between filaments caused by alternating charges.

The helical geometry of ParM filament, with 12 subunits per turn, is compatible with a hexagonal

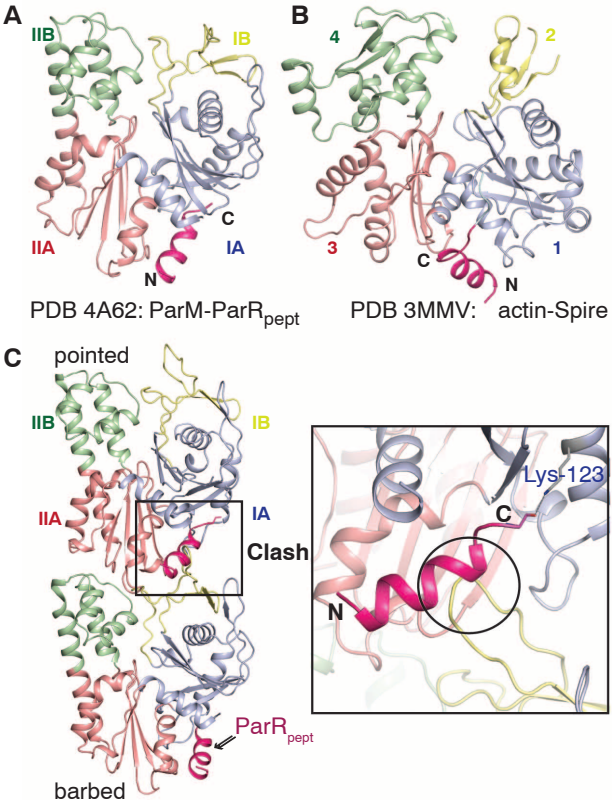

Fig. 2. ParR*C* binds at the barbed end of ParM filaments. (**A** and **B**) The $ParR_{pept}$ binding site corresponds to that of Spire on actin. The helices of the interacting proteins are shown in pink, with the rest in gray. (A) ParM:$ParR_{pept}$ (PDB ID: 4A62), (B) actin:Spire (PDB ID: 3MMV). (**C**) $ParR_{pept}$ binds at the interprotofilament interface of ParM. Two subunits of the ParM filament with hypothetical $ParR_{pept}$ at the binding sites are shown. In that position, $ParR_{pept}$ clashes with loop 37-46 from domain IB of the adjacent subunit.

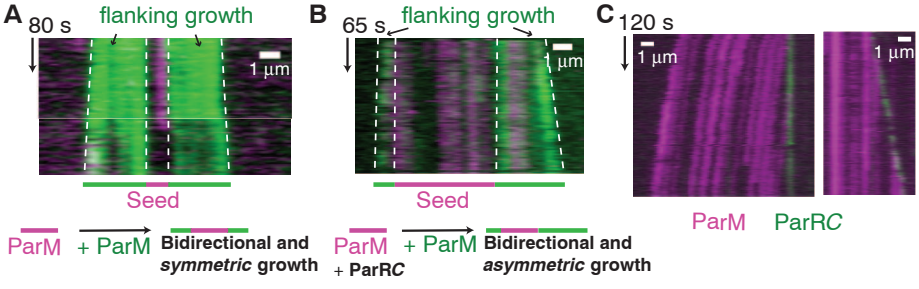

Fig. 3. ParR*C* accelerates growth at one end of ParM filaments. (**A** and **B**) TIRF microscopy kymographs of filaments in dual-label experiments (*11*) (A) without ParR*C* and (B) with ParR*C*. Growth of ParM filaments without ParR*C* is bidirectional and symmetric, with equal slopes on both ends of the kymograph, whereas addition of ParR*C* results in asymmetric growth, with unequal slopes. The relevant boundaries are highlighted. (**C**) Monomers are recruited to the ParR*C*-bound end of ParM filament. Kymograph from a filament labeled with Alexa-568 (magenta) and YOYO-1–labeled ParR*C* (green) are shown.

or square packing of ParM filaments in a bundle (fig. S5C) (*4*), in contrast to nonbundling actin filaments with a 13-monomer repeat. Bundles of ParM filaments have been observed in *E. coli* cells expressing ParM at wild-type levels (*20*) and during plasmid partitioning in vivo (*21*). Also, bundles of antiparallel ParM filaments have been described in vitro (*22*).

Antiparallel pairing explains observations of ParR*C* at both ends of ParM filaments (*9*, *10*). Of the 826 filaments we counted, 104, 540, and 182 filaments were observed with ParR*C* at zero, one, and two ends, respectively, consistent with single-end binding and pairing. Bipolar spindles of ParM were observed by TIRF microscopy using ATP. Stable filaments were seen only as elongating spindles with ParR*C* at both ends, pushing plasmids apart at a rate of 22.6 ± 4.8 monomers per s (n = 40; movies S13 and S14 and table S3). Upon loss of ParR*C* at limiting concentrations of ParM (350 to 500 nM), dynamic instability caused spindle disassembly at a rate of 100.3 ± 18.7 monomers per s (n = 61; Fig. 4F, fig. S4E, movies S15 and S16, and table S3).

To demonstrate that the spindles comprised at least two antiparallel filaments, we introduced negatively charged residues within loop 18-21 (S19E, G21E, where E indicates Glu) (Fig. 4D) to weaken the interfilament interaction through repulsive electrostatic forces. We observed spindles (n = 65) that split into the constituent filaments (movie S17 and Fig. 4G). This confirms that spindles are not formed by a single ParM

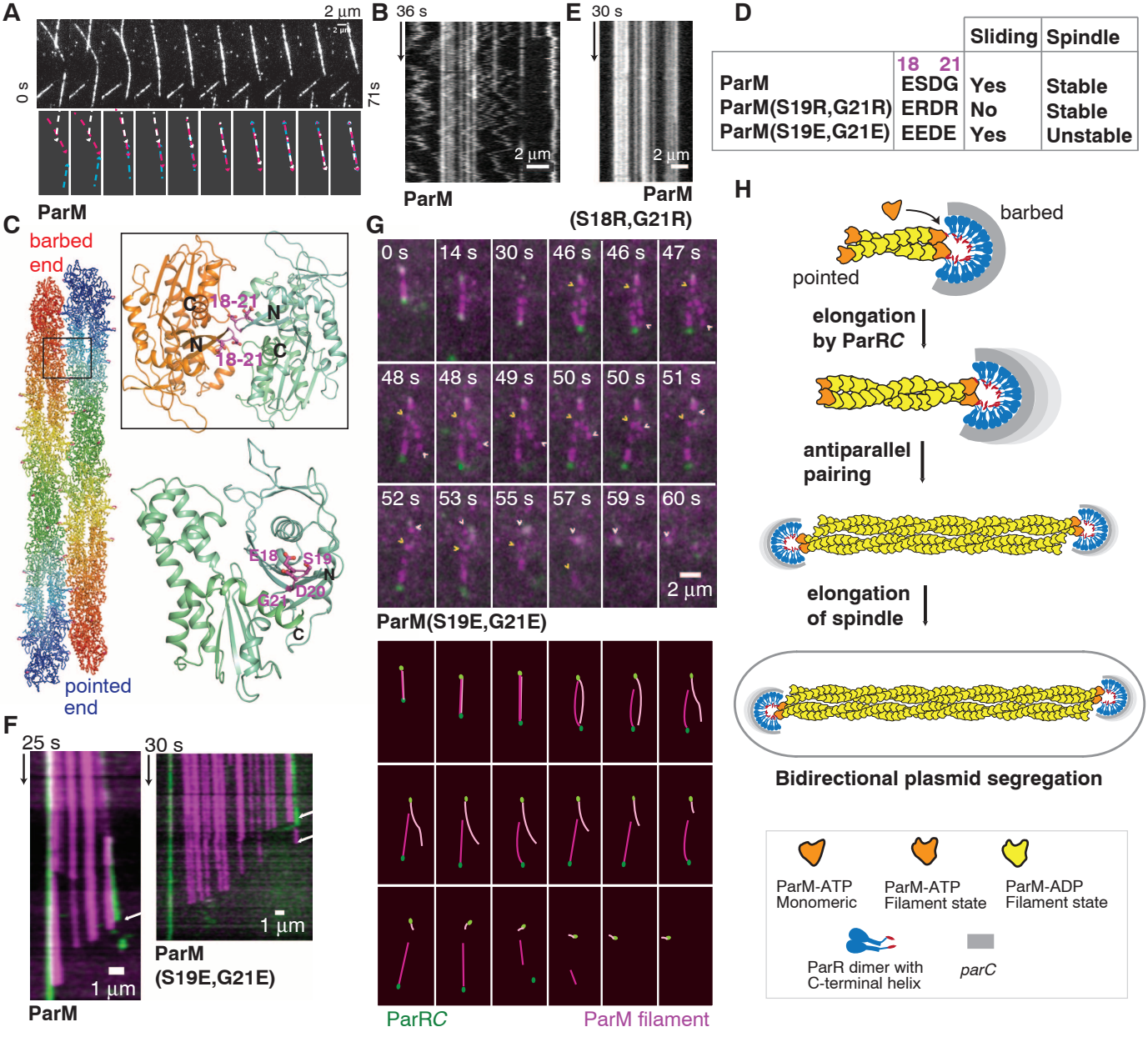

Fig. 4. A bipolar spindle comprises at least two antiparallel ParM filaments. (**A**) ParM-AMPPNP filaments condensing into a bundle (movie S7). (**B**) Kymograph of a bundle of ParM. Static filaments yield straight lines, whereas concerted zigzag motion shows sliding filament movement. (**C**) Atomic model of an antiparallel filament pair. (Inset) Interface involving loop 18-21 in the antiparallel arrangement. D, Asp. (**D**) Interface mutations and their effect on sliding and spindle stability. (**E**) Kymograph of a bundle of ParM(S19R,G21R) filaments that are static because of stronger interfilament interactions. (**F**) Kymographs of disassembling spindles of ParM and ParM(S19E,G21E). Arrows highlight the slopes of disassembly. (**G**) Montage of spindle disassembly events in ParM(S19E,G21E) mutant (movie S17). The spindle splits apart because of repulsive surface charges, demonstrating that the bipolar spindle of ParM (magenta) is formed of more than one filament. The constituent filaments with ParR*C* (green) bound at one end begin disassembly from the pointed ends. The pointed ends are highlighted with arrowheads. (**H**) Schematic representation of the bipolar spindle model (see also fig. S6).

filament, with ParR*C* attached at both ends (*9*, *10*) (Fig. 4H). ParM filaments in a spindle were protected from dynamic instability by binding of ParR*C* at the barbed end and pairing with another ParR*C*-bound filament at the pointed end (movies S15 to S19; Fig. 4, F to H; and fig. S4, E and F). The trigger for disassembly was either the loss of ParR*C* (movies S15 and S16) or exposure of pointed ends because of unwinding of the antiparallel bundle (movies S17 and S19).

These observations and previously published work (*3*, *4*) provide a comprehensive model of ParMR*C*-mediated plasmid segregation (fig. S6): a critical concentration of ATP-bound monomers in the cell nucleates ParM filaments (or nucleation is ParR*C*-mediated) (*18*). ParR*C* binding rescues the dynamic filaments from disassembly at the barbed end only. ParR*C* speeds up the growth at the barbed end by a forminlike mechanism. The free pointed end remains prone to disassembly unless it pairs up antiparallel with another ParM filament bound to ParR*C*, probably shortly after plasmid replication. Thus, a bipolar spindle of two antiparallel filaments is the minimum unit in plasmid segregation. R1 plasmid has a copy number of about six, which is about the number of filaments within bundles in plasmid-segregating cells (*20*). ParM bundles are stronger than single filaments, which is advantageous when pushing plasmids through the cytoplasm. A single bundle will also ensure concerted segregation of all sister plasmids, as observed in vivo (*21*).

The lateral interaction among dynamic filaments, as in ParMR*C*, may also facilitate contraction in other cytomotive filament systems such as FtsZ in bacterial cell division (*23*). Our model of antiparallel actinlike ParM filaments, without the necessity of bundling factors or motor proteins, provides an attractive conceptual precursor for actin contractile systems, such as muscle.

References and Notes

1. F. van den Ent, J. Møller-Jensen, L. A. Amos, K. Gerdes, J. Löwe, *EMBO J.* **21**, 6935 (2002).
2. D. Popp *et al.*, *EMBO J.* **27**, 570 (2008).
3. K. Gerdes, M. Howard, F. Szardenings, *Cell* **141**, 927 (2010).
4. J. Salje, P. Gayathri, J. Löwe, *Nat. Rev. Microbiol.* **8**, 683 (2010).
5. E. C. Garner, C. S. Campbell, R. D. Mullins, *Science* **306**, 1021 (2004).
6. E. C. Garner, C. S. Campbell, D. B. Weibel, R. D. Mullins, *Science* **315**, 1270 (2007).
7. J. Møller-Jensen, S. Ringgaard, C. P. Mercogliano, K. Gerdes, J. Löwe, *EMBO J.* **26**, 4413 (2007).
8. M. A. Schumacher *et al.*, *Nature* **450**, 1268 (2007).
9. C. L. Choi, S. A. Claridge, E. C. Garner, A. P. Alivisatos, R. D. Mullins, *J. Biol. Chem.* **283**, 28081 (2008).
10. J. Salje, J. Löwe, *EMBO J.* **27**, 2230 (2008).
11. See supplementary materials available on *Science* Online.
12. T. Fujii, A. H. Iwane, T. Yanagida, K. Namba, *Nature* **467**, 724 (2010).
13. T. Oda, M. Iwasa, T. Aihara, Y. Maéda, A. Narita, *Nature* **457**, 441 (2009).
14. T. Otomo *et al.*, *Nature* **433**, 488 (2005).
15. M. Hertzog *et al.*, *Cell* **117**, 611 (2004).
16. R. Dominguez, *Trends Biochem. Sci.* **29**, 572 (2004).
17. B. L. Goode, M. J. Eck, *Annu. Rev. Biochem.* **76**, 593 (2007).
18. J. Møller-Jensen, R. B. Jensen, J. Löwe, K. Gerdes, *EMBO J.* **21**, 3119 (2002).
19. J. Møller-Jensen *et al.*, *Mol. Cell* **12**, 1477 (2003).
20. J. Salje, B. Zuber, J. Löwe, *Science* **323**, 509 (2009); 10.1126/science.1164346.
21. C. S. Campbell, R. D. Mullins, *J. Cell Biol.* **179**, 1059 (2007).
22. D. Popp *et al.*, *Biochem. Biophys. Res. Commun.* **353**, 109 (2007).
23. S. X. Sun, S. Walcott, C. W. Wolgemuth, *Curr. Biol.* **20**, R649 (2010).

Acknowledgments: We acknowledge N. Barry and C. Johnson (MRC-LMB, help with TIRF microscopy and isothermal titration calorimetry); T. Kato (Osaka University, technical support with cryo-EM); beamline support at ID29, ID14-2 (European Synchrotron Radiation Facility, France), and I02 (Diamond Light Source, UK); L. Amos, S. Bullock, A. Carter, and R. Gasper-Schönenbrücher (MRC-LMB, critical reading of the manuscript); and K. Gerdes (Newcastle University) and A. Toste Rêgo (MRC-LMB) (provision of reagents). Support by the MRC (U105184326 to J.L.), Grants-in-Aid for Scientific Research, Ministry of Education, Culture, Sports, Science and Technology (MEXT), Japan (21227006 to K.N.), and FP7-IIF-2008 fellowship (P.G.) is acknowledged. Protein Data Bank (PDB) accession codes: ParM-AMPPNP, 4A61; ParM-AMPPNP-ParR$_{pept}$, 4A62. The EM reconstruction has been deposited in the Electron Microscopy Data Bank (EMD-1980), fitted coordinates in the PDB (4A6J).

Supplementary Materials

www.sciencemag.org/cgi/content/full/science.1229091/DC1
Materials and Methods
Figs. S1 to S6
Tables S1 to S3
References (*24*–*41*)
Movies S1 to S19

20 August 2012; accepted 12 October 2012
Published online 25 October 2012;
10.1126/science.1229091

Kinetic Responses of β-Catenin Specify the Sites of Wnt Control

Ana R. Hernández,* Allon M. Klein,* Marc W. Kirschner†

Despite more than 30 years of work on the Wnt signaling pathway, the basic mechanism of how the extracellular Wnt signal increases the intracellular concentration of β-catenin is still contentious. Circumventing much of the detailed biochemistry, we used basic principles of chemical kinetics coupled with quantitative measurements to define the reactions on β-catenin directly affected by the Wnt signal. We conclude that the core signal transduction mechanism is relatively simple, with only two regulated phosphorylation steps. Their partial inhibition gives rise to the full dynamics of the response and subsequently maintains a steady state in which the concentration of β-catenin is increased.

Kinetic analysis of chemical pathways at steady state can order the steps of a reaction sequence and identify points of control (*1*, *2*). Whether such analysis can be as successful for signaling pathways as it is for mass conversion is unclear. We applied this approach to the canonical Wnt pathway, a fundamental circuit in development and adult homeostasis. Wnt leads to stabilization and accumulation of β-catenin, which then activates transcriptional targets. β-catenin is constantly synthesized but is normally maintained at a low cytoplasmic concentration by degradation. Degradation is mediated by casein kinase 1α (CK1α) and glycogen synthase kinase 3 (GSK3), which sequentially phosphorylate β-catenin, creating a phosphodegron (*3*, *4*). The interaction between the kinases and β-catenin is mediated by two scaffold proteins, Axin1 and adenomatous polyposis coli (APC), forming the so-called destruction complex.

The mechanism by which Wnt inhibits the degradation of β-catenin is still open to debate. Because phosphorylated β-catenin decreases after Wnt stimulation, it is thought that Wnt inhibits its phosphorylation of β-catenin, thereby blocking its degradation (*3*–*5*). Inhibition has been proposed to occur by interfering with GSK3 (*6*, *7*), CK1α (*4*), or Axin (*8*, *9*). Wnt is also proposed to inhibit ubiquitylation, rather than phosphorylation (*10*). Moreover, the proposed mechanisms do not explain how β-catenin is maintained at an elevated steady-state level and what prevents it from accumulating indefinitely.

To understand how Wnt controls β-catenin, we examined cultured cells, in which the β-catenin dynamics could be accurately measured. Our analysis focused on sequential β-catenin modifications across two phases: (i) a transient phase of β-catenin accumulation and (ii) a final phase at which β-catenin concentration reaches a new, higher steady state. From a basic conservation law of enzyme kinetics, we deduced the point of Wnt action and revealed a simple core mechanism that couples the Wnt signal to the steady-state amount of β-catenin.

Continuous stimulation of cells by Wnt-3A led to distinct dynamic changes in phosphorylated and total β-catenin (Fig. 1A and fig. S1). The total amount of β-catenin increased 15 to 30 min after exposure to Wnt and reached a steady state in 2 hours that was maintained for several hours. In human colon carcinoma RKO cells, β-catenin concentration increased by a factor of 6 (from 8 ± 1 nM to 52 ± 7 nM) (Fig. 1B). By contrast,

Department of Systems Biology, Harvard Medical School, Boston, MA 02115, USA.

*These authors contributed equally to this work.
†To whom correspondence should be addressed. E-mail: marc@hms.harvard.edu